HALOGAS Observations of NGC 4559: Anomalous and Extraplanar H I and its Relation to Star Formation

Vargas, Carlos J.; Heald, George; Walterbos, René A. M.; Fraternali, Filippo; Patterson, Maria T.; Rand, Richard J.; Józsa, Gyula I. G.; Gentile, Gianfranco; Serra, Paolo

Published in:
The Astrophysical Journal

DOI:
10.3847/1538-4357/aa692c

Publication date:
2017

The Astrophysical Journal, 839:118 (14pp), 2017 April 20 https://doi.org/10.3847/1538-4357/aa692c

HALOGAS Observations of NGC 4559: Anomalous and Extraplanar H I and its Relation to Star Formation

Carlos J. Vargas[1], George Heald[2,3,4], René A. M. Walterbos[1], Filippo Fraternali[4,5], Maria T. Patterson[6], Richard J. Rand[7], Gyula I. G. Józsa[8,9,10], Gianfranco Gentile[11], and Paolo Serra[12]
[1] Department of Astronomy, New Mexico State University, Las Cruces, NM 88001, USA
[2] CSIRO Astronomy and Space Science, 26 Dick Perry Ave, Kensington, WA 6151, Australia
[3] ASTRON, The Netherlands Institute for Radio Astronomy, Postbus 2, 7990 AA, Dwingeloo, The Netherlands
[4] Kapteyn Astronomical Institute, University of Groningen, Postbus 800, 9700 AV Groningen, The Netherlands
[5] Dept. of Physics and Astronomy, University of Bologna, Viale Berti Pichat 6/2, I-40127, Bologna, Italy
[6] Department of Astronomy, University of Washington, Box 351580, Seattle, WA 98195, USA
[7] Department of Physics and Astronomy, University of New Mexico, 1919 Lomas Blvd. NE, Albuquerque, NM 87131, USA
[8] SKA South Africa Radio Astronomy Research Group, 3rd Floor, The Park, Park Rd., Pinelands 7405, South Africa
[9] Rhodes Centre for Radio Astronomy Techniques & Technologies, Department of Physics and Electronics, Rhodes University, P.O. Box 94, Grahamstown 6140, South Africa
[10] Argelander-Institut für Astronomie, Auf dem Hügel 71, D-53121 Bonn, Germany
[11] Department of Physics and Astrophysics, Vrije Universiteit Brussel, Pleinlaan 2, 1050 Brussels, Belgium
[12] INAF-Osservatorio Astronomico di Cagliari, Via della Scienza 5, I-09047 Selargius (CA), Italy
Received 2017 January 30; revised 2017 March 6; accepted 2017 March 20; published 2017 April 24

Abstract

We use new deep 21 cm H I observations of the moderately inclined galaxy NGC 4559 in the HALOGAS survey to investigate the properties of extraplanar gas. We use TiRiFiC to construct simulated data cubes to match the H I observations. We find that a thick-disk component of scale height ∼2 kpc, characterized by a negative vertical gradient in its rotation velocity (lag) of $\sim 13 \pm 5\,\mathrm{km\,s^{-1}\,kpc^{-1}}$ is an adequate fit to extraplanar gas features. The tilted ring models also present evidence for a decrease in the magnitude of the lag outside R_{25}, and a radial inflow of $\sim 10\,\mathrm{km\,s^{-1}}$. We extracted lagging extraplanar gas through Gaussian velocity profile fitting. From both the 3D models and extraction analyses we conclude that ∼10%–20% of the total H I mass is extraplanar. Most of the extraplanar gas is spatially coincident with regions of star formation in spiral arms, as traced by Hα and *GALEX* FUV images, so it is likely due to star formation processes driving a galactic fountain. We also find the signature of a filament of a kinematically "forbidden" H I feature, containing $\sim 1.4 \times 10^6\,M_\odot$ of H I, and discuss its potential relationship to a nearby H I hole. We discover a previously undetected dwarf galaxy in H I located ∼0.°4 (∼58 kpc) from the center of NGC 4559, containing $\sim 4 \times 10^5\,M_\odot$. This dwarf has counterpart sources in SDSS with spectra typical of H II regions, and we conclude that it is two merging blue compact dwarf galaxies.

Key words: galaxies: halos – galaxies: ISM – galaxies: spiral

1. Introduction

Substantial reservoirs of material have been documented to exist outside the plane of disk galaxies (Putman et al. 2012). This extraplanar material has been found at multiple wavelengths and in multiple emission sources, including X-rays (Tüllmann et al. 2006), dust (Howk & Savage 1999), Hα (Rossa & Dettmar 2003), and H I (Fraternali et al. 2002; Oosterloo et al. 2007; Heald et al. 2011), indicating gas over a wide range in temperatures and densities. Extraplanar material is likely an excellent probe of the effects of spiral galaxies on their environments, and vice versa.

It is possible that extraplanar matter could have originally been a part of the disk of the underlying galaxy, but was expelled from the disk through various energetic processes, such as supernova explosions or stellar winds from massive stars. This material could then expand, and rain back down onto the galaxy after cooling. This process is referred to as the galactic fountain mechanism (Shapiro & Field 1976). The rotation velocity of this material about the galactic center is expected to decrease with distance from the plane (Bregman 1980). This reduction in rotation velocity is generally referred to as a "lag," and is a signature of extraplanar matter. However, observations of extraplanar gas show lag magnitudes that are larger than could be reproduced with ballistic models, implying that additional mechanisms are needed to explain the behavior of this material (Collins et al. 2002; Fraternali & Binney 2006). Marinacci et al. (2011) postulated that this extra interaction could be with a hot, but slowly rotating corona of gas already residing above the disks of galaxies. Alternatively, a study by Benjamin (2002) using a hydrostatic disk model finds that pressure gradients or magnetic tension could also play a part in setting the magnitude of observed lags.

Observationally, lagging gas can be found in both edge-on and inclined galaxies. In edge-on situations, one can directly measure the vertical extent and lag in the rotational velocities of the extraplanar gas. In moderately inclined galaxies, the disentangling of extraplanar gas from disk gas is more difficult, but is possible if a detectable lag exists, as in Fraternali et al. (2002), Barbieri et al. (2005), and Boomsma et al. (2008). Additionally, in such galaxies the connection with star formation across the disks is easier to establish.

The Westerbork Hydrogen Accretion in LOcal GAlaxieS (HALOGAS) survey (Heald et al. 2011) targets 22 nearby moderately inclined and edge-on spiral galaxies for deep 21 cm observations using the Westerbork Synthesis Radio Telescope (WSRT). This survey has increased the sample of nearby galaxies for which extraplanar gas can be characterized, and one of its goals is to search for a connection between

Table 1
Parameters of NGC 4559

Parameter	Value
Hubble type	SABcd
Adopted distance	7.9 Mpc ($1'' = 38.3$ pc)
M_B	−20.07
D_{25}	11.′3
v_{max}	∼130 km s^{-1}
Total mass (virial)	$\sim 2.8 \times 10^{11}\ M_\odot$

Note. The total mass was computed using Klypin et al. (2011), and represents the virial mass of NGC 4559.

extraplanar H I and star formation, and between externally originating H I and galactic fountain gas. In this paper we present a detailed analysis of the HALOGAS data cube for the moderately inclined spiral NGC 4559. Parameters of this galaxy are given in Table 1. The Hubble type of the galaxy cited in Heald et al. (2011) is SABcd, though a kinematic influence on the H I from a bar is not apparent. The adopted distance to the galaxy, 7.9 Mpc, was obtained through the median of all Tully–Fisher distances.

A previous H I study by Barbieri et al. (2005, hereafter B05) revealed many interesting details about the gas in NGC 4559. The study found evidence of $\sim 5.9 \times 10^8\ M_\odot$ of extraplanar gas with a scale height of ∼2 kpc, rotating 25–50 km s^{-1} slower than the uniform thin disk of H I. The extraplanar gas was found to be kinematically and spatially regular throughout the galaxy. Though accretion from the intergalactic medium (IGM) could not be ruled out, the regular extent of extraplanar gas suggests that it is likely due to a widespread phenomenon, such as star formation across the disk. B05 used 3D tilted ring models to model the extraplanar gas, where the thick disk had a separate rotation curve from the thin disk. We build upon this result by constraining the magnitude of vertical lag, rather than computing a separate rotation curve for the extraplanar gas. B05 also found evidence for a large H I hole at $\alpha = 12^h36^m4^s$, $\delta = 27°57'7''$, that would require $\sim 2 \times 10^7\ M_\odot$ of H I to fill. They determined the H I distribution to be highly asymmetric between the approaching and receding halves of the galaxy. Interestingly, B05 also found evidence for a stream of gas located at "forbidden" velocity in the position–velocity diagram for the major axis, near the center of the galaxy, which they postulate to be associated with the aforementioned H I hole. We further the discussion on the possible origins of this forbidden velocity feature and its possible relation to the hole.

The aim of this work is to expand upon the analysis done by B05 using the more sensitive HALOGAS observations of the same galaxy, together with ancillary Hα and *GALEX* FUV observations as tracers of star formation activity. We present the data in Sections 2 and 3, explore three-dimensional tilted ring models to characterize the presence of extraplanar gas in Section 4, and determine the mass and relation to star formation of the extraplanar gas in Section 5. In the remainder of Section 5 we further characterize the forbidden gas feature discovered in B05 and discuss its potential origins and connection to the nearby H I hole. Section 6 discusses a new detection of H I in a nearby dwarf companion galaxy, while Section 7 concludes the paper with a discussion of the results.

2. Data Acquisition and Reduction

A brief overview of the data collection and reduction process is included. We refer the reader to Heald et al. (2011) for a comprehensive description.

We used the HALOGAS survey observations of NGC 4559, taken in the Maxi-short WSRT configuration, with baselines ranging from 36 m to 2.7 km to maximize sensitivity to faint, extended emission. Nine of the ten fixed antennas were used with a regular spacing of 144 m. The total bandwidth of 10 MHz was split into 1024 channels (2.06 km s^{-1} per channel) with two linear polarizations.

We used Miriad (Sault et al. 1995) to perform the data reduction. Data properties are included in Table 2. We produced multiple data cubes using a variety of weighting schemes. The cubes were Hanning-smoothed to obtain the final velocity resolution of 4.12 km s^{-1} per channel and a beam size of $28.''38 \times 13.''10$. The 1σ rms noise in a single channel of the full-resolution cube is 0.17 mJy beam^{-1}. The minimum detectable column density (5σ and 12 km s^{-1} velocity width) of the full-resolution cube is 3.67×10^{19} cm^{-2}. The data cube with the widest field has 1024×1024 pixels of size $4''$, giving it a field of view of $68'$. The galaxy emission is much smaller than that, so we trim the field of view to $\sim 24'$ due to considerations of data size.

We note the existence of strong solar interference in the data cube of NGC 4559. The observations of this galaxy were taken in ten 12 hr blocks from 2011 January through May. This was a period of moderately large solar activity. Five out of the ten tracks were taken in May, with 3.75–5.1 hr of exposed sunlight time. Though the angular separation between the galaxy and the Sun was kept as large as possible (∼120°), there is still solar interference affecting the short baselines. This solar interference was flagged in problematic baselines and timeframes during the data reduction. The flagging reduced inner UV coverage, which lessens the sensitivity to extended, faint emission. Furthermore, artifacts from the remaining solar interference preclude the cleaning of the data cube to reach the deepest possible noise level of the HALOGAS data. We consider this solar interference to be the most likely explanation for the lack of appreciable improvement in sensitivity to extended emission over B05. However, we also note that the rms noise per channel is improved by a factor of ∼2 over B05, so we have improved point-source sensitivity, despite the lack of sensitivity to extended emission.

To improve sensitivity to faint, extended emission, we smoothed the original HALOGAS data cube to a $30'' \times 30''$ beam, making the noise level in a single channel 0.24 mJy beam^{-1}, or 0.16 K. See Table 2 for details of the $30'' \times 30''$ beam cube. The cube was corrected for the primary beam using the Miriad task "linmos" when calculating total H I mass. We use the $30'' \times 30''$ cube for all tilted ring modeling. Moment maps were created using the "moments" task within the Groningen Image Processing System (GIPSY; van der Hulst et al. 1992). Moment maps were created by first smoothing the original cube to $60'' \times 60''$, with which masks at the 5σ level were produced and applied to the full-resolution cube.

GALEX FUV and ground-based Hα images allow us to investigate in more detail the correlation between the lagging H I layer and star formation in NGC 4559. The *GALEX* FUV image from Gil de Paz et al. (2007), and a continuum-subtracted Hα image are included in our analysis. The Hα

Table 2
Observational Parameters

Parameter	Smoothed Cube	Full-resolution Cube
Synthesized beam FWHM	$30'' \times 30''$	$28\farcs38 \times 13\farcs10$
Conversion factor	0.673 K mJy^{-1}	1.630 K mJy^{-1}
Velocity resolution	4.12 km s^{-1}	4.12 km s^{-1}
rms noise per channel	0.24 mJy beam^{-1}; 0.16 K	0.20 mJy beam^{-1}; 0.26 K
Minimum detectable column density (5σ)	1.81×10^{19} atoms cm^{-2}	3.67×10^{19} atoms cm^{-2}

Note. The minimum detectable column density is calculated for a source included in three channels ($\sim$12 km s^{-1}) at 5σ. The total integration time of the observations spanned 10×12 hr. See Heald et al. (2011) for further discussion of parameters.

image was taken by one of the authors (M.P.) on 2012 March 21, with the Kitt Peak National Observatory (KPNO) 4 m telescope. The Hα exposure time was 30 minutes. The mosaic instrument is known to produce artifacts in which bright stars may appear in multiple CCDs. We first removed this crosstalk between CCDs and trimmed the image. The image was bias-subtracted, flat-fielded with dark sky flats, and stacked from dithered images. The image was then continuum-subtracted with an *R*-band image of 10 minute exposure taken on the same night. The pixel scale of the Hα image is $0\farcs258$ per pixel.

3. H I Mass and Extent of the H I Disk

We estimate the total H I mass using the primary-beam-corrected and masked total H I map and assume that the emission is optically thin. We use the standard conversion to column density, where the HPBW (half-power beam width) major and minor axes of the beam, *a* and *b*respectively, are in units of arcseconds: $N(\mathrm{cm}^{-2}) = 1.104 \times 10^{21} \times F(\mathrm{mJy\ beam}^{-1}\ \mathrm{km\,s}^{-1})/(a \times b)$. The total H I mass obtained from the HALOGAS data cube is in very good agreement with that found in B05 when the same distance is assumed: $4.53 \times 10^9\,M_\odot$ versus $4.48 \times 10^9\,M_\odot$ in B05 using our assumed distance of 7.9 Mpc. As mentioned in B05, this agrees with alternative and single-dish measurements of the mass from Broeils (1992) and Shostak (1975). This shows that the increase in integration time and sensitivity of the HALOGAS observations did not discover a larger amount of H I that the observations of B05 were not sensitive enough to probe.

We analyze the extent of the H I disk and radial profile in the highest-resolution data cube with a beam size of $28\farcs38 \times 13\farcs10$. The masked, high-resolution cube is integrated over the velocity axis to produce the total H I image, or integrated H I map shown in the top panel of Figure 1. We use the GIPSY task *ELLINT* to create azimuthally averaged surface brightness profiles for the receding and approaching halves independently. *ELLINT* is a 2D ring-fitting code that uses a least-squares fitting algorithm to constrain the H I density profile. We provide the moment 0 map as input to *ELLINT* and fit only the surface brightness profile in the approaching and receding sides, independently. We fix the position angle, inclination, and central position using the values quoted in Table 1 of B05 ($-37\fdg0$, $67\fdg2$, α(J2000) = $12^{\mathrm{h}}35^{\mathrm{m}}58^{\mathrm{s}}$, and δ(J2000) = $27°\,57'32''$ respectively) for the *ELLINT* calculation of the surface brightness profile. The inclination and position angle were both derived from the morphology and kinematics of the analysis using a tilted ring model done in B05. The central position was also tabulated by B05 using the kinematics of their H I data, and represents the kinematical center of NGC 4559. This is then converted into the column density profiles shown also in Figure 1.

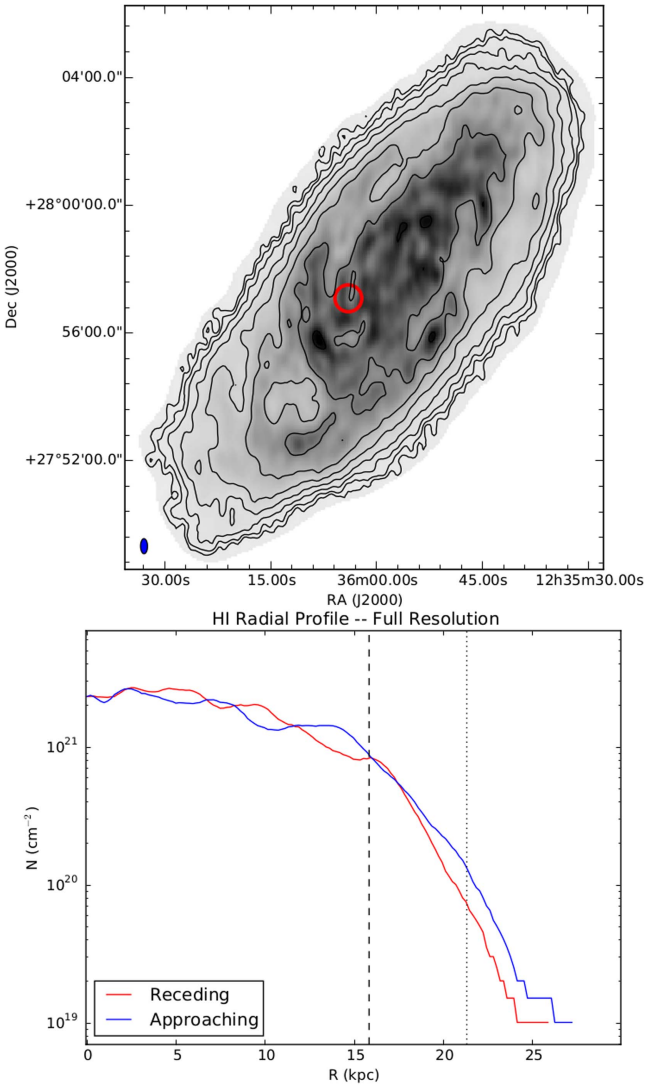

Figure 1. Top: integrated H I map of the highest-resolution HALOGAS data cube for NGC 4559. Column density contours begin at 2.4×10^{19} atoms cm^{-2} and increase in multiples of 2. The red circle marks the location of an H I hole discussed further in Section 5.2. Bottom: radial profile obtained from the highest-resolution integrated H I map. The vertical dashed line represents R_{25} of the galaxy, and the dotted vertical line is the largest radius at which B05 detects H I, as quoted in that text, and adjusted to our assumed distance of 7.9 Mpc.

The HALOGAS data are somewhat deeper than the data from B05. In Figure 1, the radial extent is similar to that found in B05. We calculate the minimum detectable column density

in the 30″ smoothed cube to be 1.81×10^{19} cm^{-2} (see Table 2), which is 1.6 times lower than the minimum detected column density from the 26″ cube in B05: 3.0×10^{19} cm^{-2}. Also, had B05 smoothed their 26″ cube to 30″, this difference would be slightly smaller. Furthermore, when the same distance is assumed, the HALOGAS data produced an extremely similar total H I mass to B05, implying that there is not much extra diffuse H I in the HALOGAS data that was not captured by B05. If we assume there exists a plateau of H I at our limiting column density due to the solar radio-frequency interference (1×10^{19} atoms cm^{-2}), ranging a radial distance between 25 and 30 kpc from the center of the galaxy, there would be only $\sim 7 \times 10^7 M_\odot$ of extra H I to detect.

We do not detect a sharp cut-off in H I but see a rather constant slope in log (column density) down to the last detected point at $\sim 1 \times 10^{19}$ atoms cm^{-2}. A cutoff might be expected due the intergalactic ionizing radiation field, as was found in M83 (Heald et al. 2016). However, this effect would appear near a column density of a few times 10^{19} atoms cm^{-2} (e.g., Corbelli & Salpeter 1993; Maloney 1993), which is near our sensitivity limit. We also note the clear change in H I profile morphology inside and outside R_{25}. Within R_{25} the H I profile seems clumpy and oscillates, perhaps due to overdensities such as spiral arms. Outside R_{25} the H I distribution becomes more uniform.

Given the high theoretical sensitivity of the HALOGAS data cube, it is surprising that the radial profile of H I column density does not reach fainter levels. We suspect this is due to the effects of solar interference on the observations (see Section 2). The deconvolution process of the HALOGAS data is imperfect and cannot fully recover the lack of short spacings. In particular, we can detect slightly negative and positive residuals due to solar interference on large angular scales in individual cleaned channel maps at the level of $\sim 1 \times 10^{18}$ atoms cm^{-2}. These residuals change in depth and location between channel maps, and the summation of channels will then limit the sensitivity in the integrated H I map. If these residuals are summed over about three channels at 3σ, this limiting column density would approach $\sim 1 \times 10^{19}$ atoms cm^{-2}, the lowest column densities we observe in the integrated H I radial profile. It is likely that a combination of the HALOGAS data with observations of NGC 4559 using the Green Bank Telescope (GBT) would lead to detection of lower column densities. An effort along these lines is underway using observations with the GBT (N. Pingel et al. 2017, in preparation).

4. Tilted Ring Models

There are various signs of vertically extended lagging gas within the HALOGAS data cube itself. In Figure 2, we show the channel maps of the 30″ resolution HALOGAS cube, rotated so the major axis is horizontal. Signs of lagging extraplanar gas can be seen as emission that fills the "C"-shaped channel maps at intermediate velocities.

Since the analysis in B05 was done, the vertical velocity structure has been measured in edge-on galaxies, such as NGC 891 (Kamphuis et al. 2007; Oosterloo et al. 2007). Such studies have found that the lagging component is characterized by a vertical gradient in velocity, rather than a bulk decrease in velocity with a separate rotation curve from the disk, making the velocity gradient the preferred characterization. Thus, in this study, we constrain the magnitude of the velocity gradient. This is an improvement over B05, where a separate rotation curve for the thick disk was used. To accomplish this, we use TiRiFiC (Józsa et al. 2007) to create 3D tilted ring models to match to the HALOGAS data cube. TiRiFiC is a stand-alone program that constructs 3D simulated data cubes of rotating galactic disks. In addition to standard capabilities in other tilted ring codes, TiRiFiC allows for the addition of simple radial and vertical inflows and outflows in the construction of the simulated cubes. We present diagnostic position–velocity diagrams and channel maps of the 3D models as compared to the data in Figure 3.

We reproduce the "lagging" model from B05 as a point of comparison. This model contains a two-component gas layer with a thin disk of 0.2 kpc and a thick disk of 2 kpc. The two disks have separate rotation curves, with the exact values as presented in Figure 7 of B05. The radial profile of surface brightness was reproduced from Figure 3 of B05, and 10% of the total was put into the thick disk, as was found in B05. The B05 model is included in the leftmost column in Figure 3.

We create new 3D models to match to the HALOGAS data cube. We use the GIPSY tasks *ELLINT* and *ROTCUR* to find initial estimates for the surface brightness profile and rotation curve. Both tasks are 2D ring-fitting codes that use a least-squares fitting algorithm to constrain the H I density profile (*ELLINT*) and the rotation curve (*ROTCUR*).

We use *ELLINT* in the same fashion here as for the calculation of radial profile in Section 3. In a similar fashion, we provide the moment 1 map (velocity field) as input to *ROTCUR*, and fit only the rotation curve in the approaching and receding halves of the galaxy, independently. In the *ROTCUR* fitting of the rotation curve, we fix the position angle, inclination, central position, and systemic velocity using the values quoted in Table 1 of B05. In both tasks we use 61 rings, all of thickness 15″. We used the initial output surface brightness profile and rotation curve from *ELLINT* and *ROTCUR* as the initial input parameters to TiRiFiC to produce 3D tilted ring models. In TiRiFiC, the values of inclination angle, central position angle, and central position are the same throughout all models and are 67°, −37°, and $12^h35^m58^s$ +27° 57′32″, respectively. The approaching half also seems to show a slight warp at large radii. So, the position angle was lowered, through trial and error, by 4°, beginning at a radius of 18.3 kpc, in that half of the galaxy.

Minor adjustments were made to the *ELLINT* and *ROTCUR* output surface brightness profile and rotation curve. These adjustments were made interactively, through trial and error, using TiRiFiC to better match the full 3D structure of the data cube. In all subsequent 3D models, we use trial and error to optimize each parameter by comparing the model to the channel maps, the position–velocity diagrams along both the major and minor axes, the moment 0 map, and the moment 1 map of the 30″ × 30″ cube. We do not use TiRiFiC in automated fitting mode, because conventional fitting routines fail to adequately fit faint structures. Since this study is most interested in characterizing faint structures, such as diffuse lagging extra-planar gas and the forbidden gas stream, we elect to fit the cube in this manner. The rotation curve we adopted for all models overlaid on the position–velocity diagram along the major axis and the column density profiles are included in Figures 4 and 5.

We experimented with various warp morphologies by varying the inclination near the edges of the disk, and the scale height in an attempt to reproduce the signatures of lagging

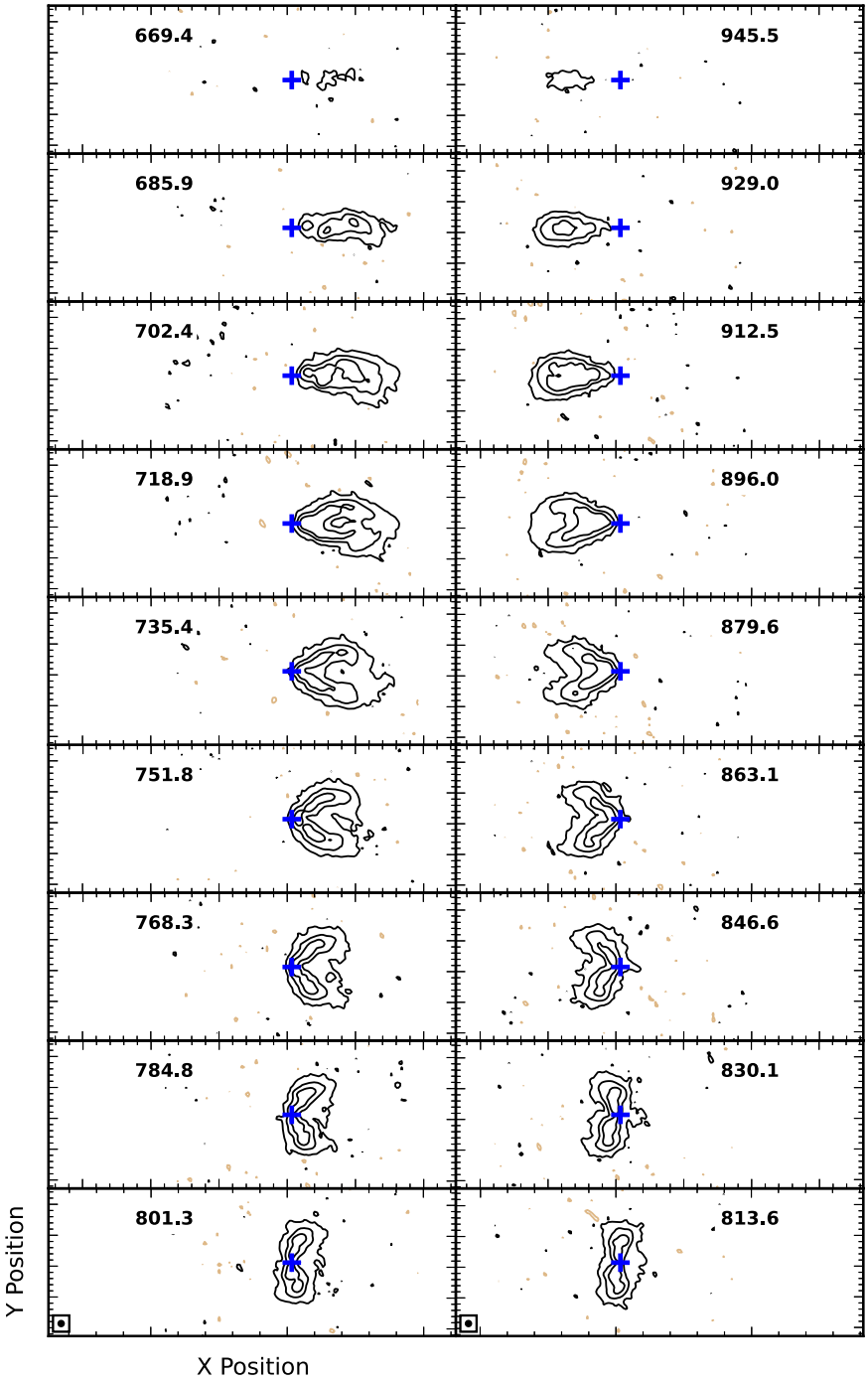

Figure 2. Channel maps for the HALOGAS data cube smoothed to a $30'' \times 30''$ beam and rotated 123° to make the major axis horizontal. The kinematic center of the galaxy is marked with a blue cross and the velocity of each channel, in km s^{-1}, is included. In this plot and all following channel maps, the right and left columns are the receding and approaching halves, respectively. Contour levels are −3.03, 3.03, 27.3, and 106.1 ($\times 10^{18}$ cm^{-2}). The negative contour is colored light brown. Large tick marks are spaced by $1'$ and $3'$ on the X and Y axes, respectively.

gas. One such signature can be seen in the position–velocity diagram along the major axis as diffuse emission that is found at velocities closer to systemic than the normally rotating disk. This extraplanar gas feature is commonly referred to as "beard gas." No amount of disk warping or disk thickness alone could reproduce the data adequately.

We then added a thick-disk component to the first models with a uniform lag throughout. The following parameters were adjusted and matched to the data through trial and error: thick-disk scale height, thick-disk lag, percentage of total gas in the thick disk, and global velocity dispersion. The velocity dispersion was constrained primarily by matching the thickness and spacing of brightness contours in the position–velocity diagram along the major axis and channel maps. The resulting parameters are shown in Table 3, and the model itself can be seen in the second column of Figure 3.

To better illustrate how constrained the key parameter of lag is in this model, we produce two additional models that are identical to the uniform lag model, but with a lag of ± 5 km s^{-1} kpc^{-1}. We note that the lag value is degenerate

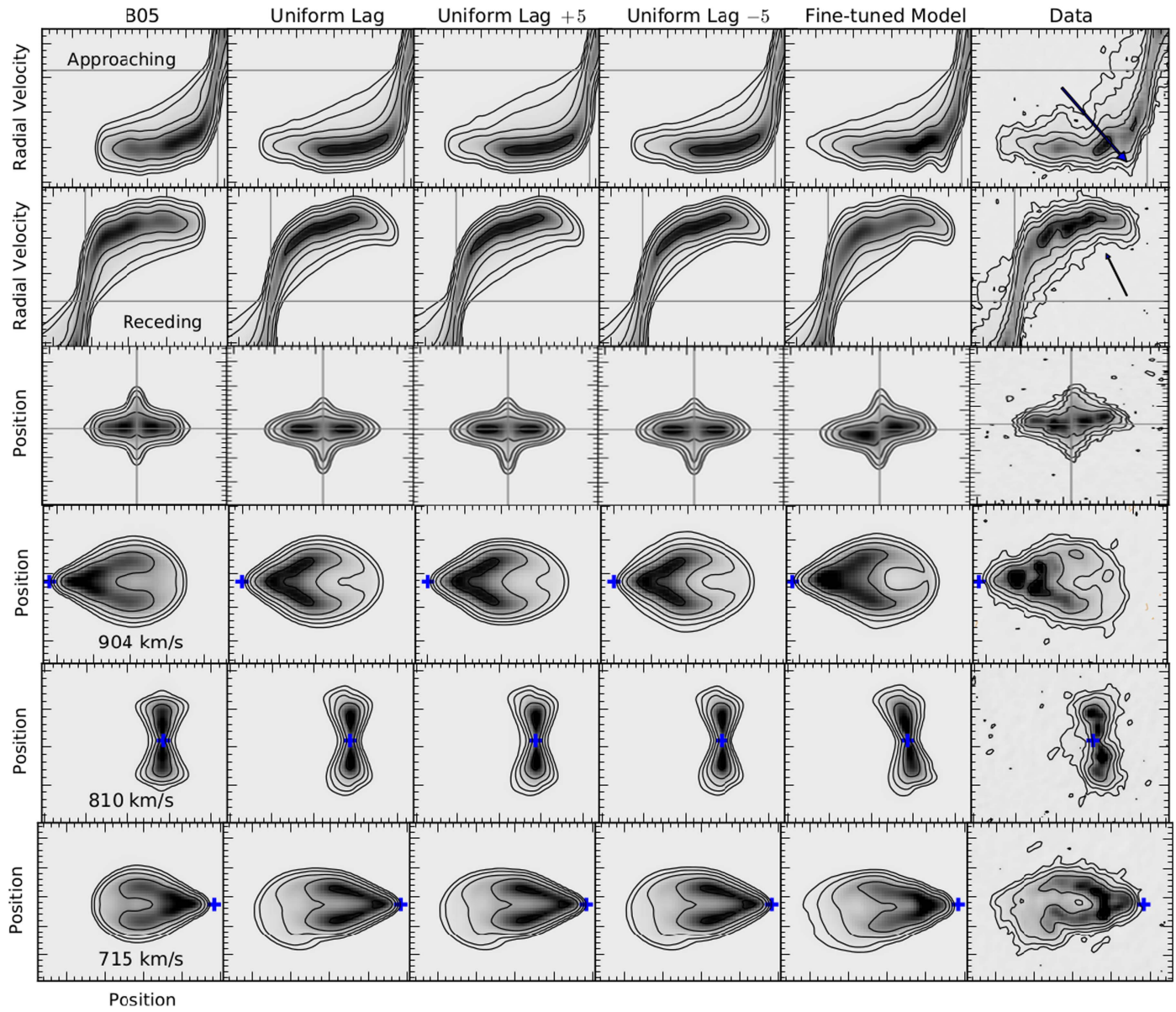

Figure 3. All 3D tilted ring models and data. First row: position–velocity diagram along the major axis zoomed in on the lower-velocity approaching side. Second row: position–velocity diagram along the major axis zoomed in on the higher-velocity receding side. Third row: position–velocity diagram along the minor axis. Fourth through sixth rows: channel maps at the velocity marked in the panels in the first column. All channel maps are rotated to have the major axis horizontal. All panels have the same contour levels, which begin at 2σ and increase in multiples of 3, where $\sigma = 0.24$ mJy beam^{-1}. Negative contours are plotted for the data in light brown at -2σ. Large x-axis tick marks in the top three rows are separated by 8 kpc, and the y-axis tick marks are separated by 50 km s^{-1}. In the channel maps, large ticks are separated by 7 kpc. The arrows in the position–velocity diagrams along the major axis mark regions of specific interest when fitting radially dependent velocity dispersion and lag magnitudes (see Section 4). The vertical and horizontal gray lines in the top three rows mark the central position and systemic velocity. The blue + marks in the channel maps mark the kinematic center of the galaxy.

with other parameters of the model, such as the thick-disk scale height and velocity dispersion (see Section 4.1). These two new models are shown in the third and fourth columns of Figure 3.

In a final model, referred to as the fine-tuned model, we experimented with various values of velocity dispersion and lag in each individual ring.

We converged on a model containing three values of velocity dispersion in three radial extents. For $R \leqslant 3.4$ kpc, the velocity dispersion is 25 km s^{-1} in the receding half of the thin disk. For 3.4 kpc $< R <$ 12.0 kpc the dispersion is 18 km s^{-1}. Beyond 12.0 kpc, the velocity dispersion is 10 km s^{-1}. This can likely be attributed to turbulent motions in central star-forming regions. In the approaching half, rings at $R = 2.8$ kpc and $R = 3.4$ kpc of the thin disk contain 25 km s^{-1} of velocity dispersion, to account for the "bump" in the position–velocity diagram (see arrow in first row, Data column in Figure 3). We also increase the lag in the receding half to 13 km s^{-1} kpc^{-1} for $R <$ 12.0 kpc of the thick disk, which roughly corresponds with R_{25}. The rest of the thick disk in the receding half of the galaxy contains no lag in this model due to a sharp cutoff in signatures of extraplanar gas in the position–velocity diagram along the major axis (see arrow in second row, Data column in Figure 3). We note that this lack of lag at large radii is not indicative of a sharp radially shallowing lag, but is mostly due to the lack of extraplanar gas at those radii in the receding half.

The approaching half of the galaxy has a uniform lag throughout in this model, just as in the previous model. Lastly, we include a modest radial inflow along the entirety of the thin

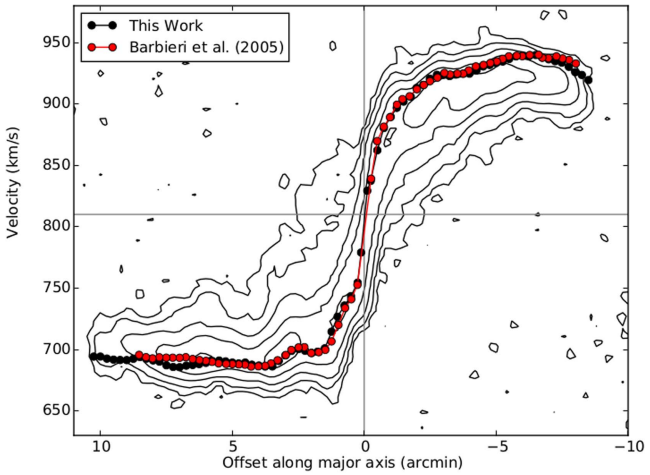

Figure 4. Rotation curves of the best-fitting thin-disk model (black) and the model of Barbieri et al. (2005) (red) overlaid atop the position–velocity slice along the major axis. Contours begin at 2σ and increase in multiples of 3. From left to right, this figure moves along the major axis following from southeast to northwest as seen on the sky. Values of the rotation curve are shown at the inclination of the galaxy. A gas feature at forbidden velocity can be seen in the top left quadrant and is discussed further in Section 5.2.

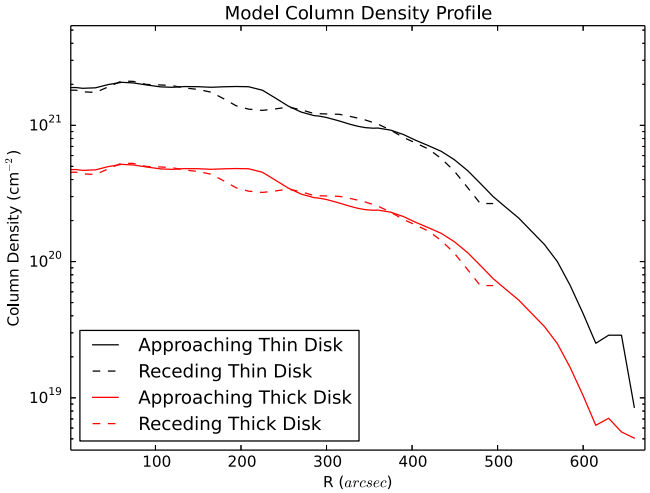

Figure 5. Column density profile for each component of the thick-disk model.

disk of 10 km s^{-1} in order to better match a kink in the position–velocity diagram along the minor axis. We note that inside a radius of 10 kpc, radially inflowing gas with this velocity would reach the center of the galaxy within a gigayear. This model is shown in the fifth column of Figure 3.

The uniform lag model captures much of the lagging gas component, as seen in the above-described signatures of extraplanar gas. However, that model requires different lag magnitudes between the approaching and receding halves. Differences between the uniform lag model and that same model with increased and decreased lags (columns two through four of Figure 3) are mostly seen in the diffuse signatures of extraplanar lagging gas contours in the position–velocity (p–v) diagram along the major axis (columns one and two).

The fine-tuned model with its small-scale variations in velocity dispersion and lag best represents both halves of the galaxy. From this analysis it is apparent that the lag magnitude does not change from one half of the galaxy to the other, but does cut off at large radii in the receding half, far from the star-forming disk. This result supports a galactic fountain model for extraplanar lagging gas, since the lag magnitude is uniform throughout the star-forming disk, and drops off at the edge. Note that no model adequately represents the forbidden gas. See Section 5.2 for a brief discussion on modeling the forbidden gas component. Also note that all asymmetries in the fine-tuned model that do not exist in other models arise from the specific treatment of lag, velocity dispersion, and the modest radial inflow that we include exclusively in that model.

The B05 model is quite comparable to the uniform lag model. We claim that a uniform lag can explain lagging gas just as adequately as two distinct rotation curves for the thin and thick disks in NGC 4559. A uniform lag is preferable in that it has been observationally shown to be more physically accurate (Kamphuis et al. 2007).

Zschaechner et al. (2015) discuss trends in lags among other galaxies and find that lags seem to reach their radially shallowest values near R_{25}. In the fine-tuned model, we model the lag in the receding half of NGC 4559 to cut off sharply at a radius of 12.06 kpc. At our assumed distance ($D = 7.9$ Mpc), R_{25} is 12.98 kpc, which makes this cutoff in radial lag at $0.93R_{25}$. So, this result is consistent with what was found in Zschaechner et al. (2015). Tilted ring models were created from the HALOGAS data cube of NGC 4559 including radially varying lags, but no radially varying lag producing appreciable improvement over the fine-tuned model. As discussed in Zschaechner et al. (2015), the overall steepness of lags suggests that conservation of angular momentum is not a sufficient explanation. Also, Marinacci et al. (2011) create simulations of fountain gas clouds moving through a hot halo medium, and are better at reproducing the steepness of lags seen observationally. Alternatively, Benjamin (2002) propose that pressure gradients could explain the magnitude of lags, but this has been difficult to accomplish observationally. Deep radio continuum observations with the recently upgraded Very Large Array, such as Irwin et al. (2012), should make future measurements of nonthermal pressure gradients possible.

4.1. Uncertainties in Derived Parameters

In general, uncertainties in three-dimensional tilted ring parameters that describe the data are estimated by varying each individual parameter to the point where the model no longer adequately represents the data (Gentile et al. 2013). Certain projections or regions in the data cube are more sensitive to some parameters than others, so these intricacies are considered in estimating uncertainties. The decisions as to what constitutes improvements and acceptable models were based on visual inspection of the various plots, as in previous papers in this type of work. The subtle features of low column density generally do not typically lend themselves easily to statistical measures but visual inspection shows clearly whether a certain model feature is required to reproduce particular faint features in p–v diagrams and channel maps.

A comparison between total H I maps is effective at determining the uncertainty in inclination and position angle. A change of 3° in both inclination and position angle through the complete disk is enough to make the total H I maps inconsistent with the data.

To constrain the uncertainty in global velocity dispersion, we analyze position–velocity diagrams. After testing this parameter,

Table 3
Tilted Ring Fitting Parameters of NGC 4559

Parameter	Uniform Lag Model	Fine-tuned Model
Thin-disk scale height	200 pc	200 pc
Thick-disk scale height	2 kpc	2 kpc
Central position angle	$-37\overset{\circ}{.}0$	$-37\overset{\circ}{.}0$
Central inclination	$67\overset{\circ}{.}2$	$67\overset{\circ}{.}2$
Kinematic center (α, δ, J2000)	$12^{h}35^{m}58^{s}$ $+27°57'32''$	$12^{h}35^{m}58^{s}$ $+27°57'32''$
Thick-disk lag magnitude	Approaching: 13; receding: 6.5 km s^{-1} kpc^{-1}	Approaching: 13; receding: 0–13 km s^{-1} kpc^{-1}
Global velocity dispersion	10 km s^{-1}	10 km s^{-1} + (0–15) km s^{-1}
Percentage gas in thick disk	20%	20%
Vertical density profile	sech^2 + sech^2	sech^2 + sech^2

Note. Central position angle describes the inner, unwarped section of the disk. The fine-tuned model contains all of the same global properties as the thin + thick disk model, and has variable values for thick-disk lag magnitude and velocity dispersion. See the text for details on variable parameters in the fine-tuned model.

the high-velocity contours in the position–velocity diagram along the major axis no longer represent the data when changed by more than ± 3 km s^{-1} from their original value of 10 km s^{-1}. We note that the velocity dispersion in the extraplanar gas is degenerate with the thick-disk scale height and the magnitude of the thick-disk lag. We account for this degeneracy as well as possible in estimating this uncertainty.

Uncertainties in parameters related to extraplanar gas are also estimated. We assume a thin-disk scale height of 200 pc, while varying values were used for the thick disk. The fitting done in B05 assumed a thin-disk scale height of 200 pc, so, for consistency, we retain that value, despite the resolution limits on constraining that number present in both studies. The central channels in the data cube are particularly sensitive to changes in scale height. We find that the thick disk must have a scale height of 2 ± 1 kpc. Since NGC 4559 is not seen edge-on, the relative mass and amplitude of lag for the extraplanar gas are not easily constrained. We find between 15% and 25% of the total H I mass in extraplanar gas. We find the uncertainty in lag to be $\sim$5 km s^{-1} kpc^{-1} in both halves of the galaxy. These uncertainties take the degeneracy between scale height and lag magnitude into account. For instance, large values of scale height can be compensated with small lag magnitudes and vice versa. However, small imperfections in models, such as location of signatures of extraplanar gas in the position–velocity diagram along the major axis and thickness of diffuse emission in channel maps, were closely inspected to minimize this degeneracy.

5. Anomalous Gas Extraction

It is useful to separate the lagging extraplanar gas component from the total H I data cube in an independent way. To that end, we follow the procedure by Fraternali et al. (2002) to extract the extraplanar gas component, and create two separate data cubes: one with emission attributed to regularly rotating gas, and another with only emission of extraplanar gas. This procedure was also done in B05, so we will focus on comparing our new results with tracers of star formation.

This procedure assumes that each H I line profile contains a narrow Gaussian-shaped component whose peak is positioned close to the rotation velocity, and a broader component whose peak is closer to the systemic velocity. The latter is attributed to extraplanar lagging gas whose profile's shape is unconstrained, but likely substantially fainter than the normally rotating component. We estimated the contribution of the normally rotating component by fitting a Gaussian profile to the upper portions of the total line profile. Modeling only the tops of the line profiles enables us to minimize contamination from potential abnormally rotating components. Experimentation using various percentages of line profiles was performed to decrease the occurrence of fitting artifacts. The procedure produced the fewest artifacts when only the upper 60% of each line profile was fit. The amplitudes, central velocities, and widths of the Gaussian profiles were fit throughout the data cube. Based on experimenting with parameters, a dispersion maximum limit on each Gaussian profile of 30 km s^{-1} was imposed on the fitting. The Gaussian profile fit to each line profile was then subtracted from the data line profiles, leaving only anomalously rotating extraplanar gas. In 285 out of 158,234 instances, Gaussian profiles could not be fit. In these instances, the profiles were excluded from the extraplanar cube.

The results of the extraplanar gas extraction can be seen in Figures 6 (right panels) and 7. The behavior of the extraplanar gas seen in velocity fields is somewhat more irregular than that in the total data. As seen in the bottom right panel of Figure 6, the residual p–v diagram from the fit (i.e., the presumed extraplanar gas) includes some gas at extreme values of radial velocity, near $\sim$950 km s^{-1} and $\sim$675 km s^{-1}, which is not lagging. This is due to the limitation imposed by forcing the fit to only 60% of the peak of the profile and the maximum cap on the velocity width of the regularly rotating thin disk in the fit. This gas is also likely due to the assumption of Gaussian velocity profiles. If the gas is clumpy or moving peculiarly the assumption of Gaussian profiles is incorrect. However, most of the residual gas is indeed lagging, because we find $\sim$10% of the total residual to reside in the extreme velocity regimes of the position–velocity diagram along the major axis.

Assuming the H I emission is optically thin, we can estimate the total mass in H I from its emission. The total H I mass of the galaxy is $\sim 4.5 \times 10^9 M_\odot$. The mass of the extracted extraplanar H I is $\sim 4.0 \times 10^8 M_\odot$, or $\sim$10% of the total H I mass. The mass in the model with a thick H I disk derived from the fitting analysis for a tilted ring contains 20% of the total H I mass. However, the two methods are not directly comparable since the portion of that thick disk at low z was superimposed over the thin disk in the ring models. Since the vertical profile used in the ring modeling was a sech^2 model, one can integrate that function over the thin-disk scale height, and exclude that amount of gas in the thick disk that spatially resides within the thin disk. The amount of thick-disk mass outside ± 3 times the thin-disk scale height is 14% of the total mass. This is still somewhat more than for the extracted emission in the Gaussian fitting. In reality, the method of line profile fitting certainly

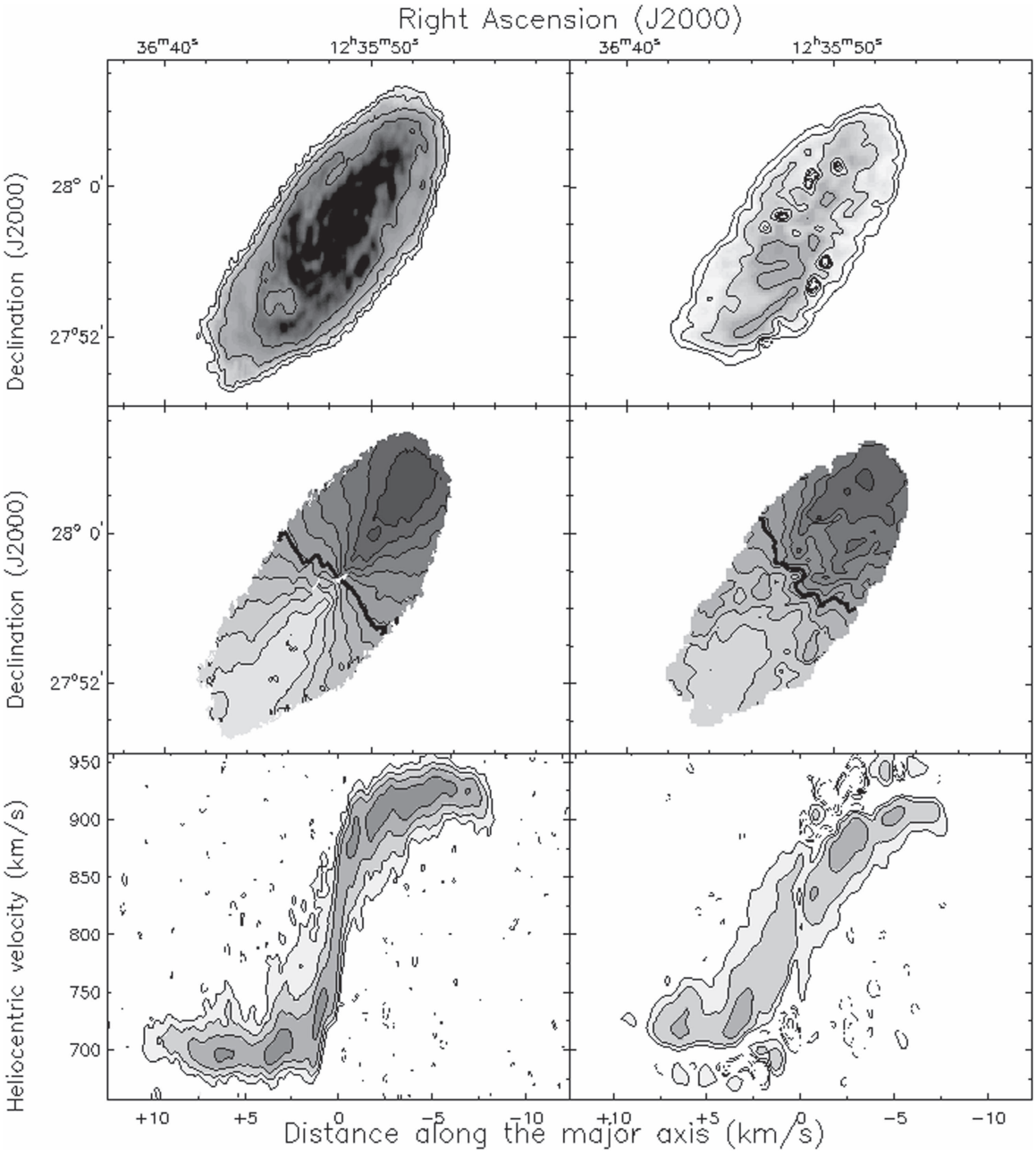

Figure 6. Various plots of the results of extraplanar gas extraction. Upper left: integrated H I map of the data, upper right: integrated H I map of the extracted extraplanar gas, middle left: velocity field of data, middle right: velocity field of extracted extraplanar gas, lower left: position–velocity slice along the major axis of the data, lower right: position–velocity slice along the major axis of the extracted extraplanar gas. All column density contours begin at 3σ in each respective cube and increase in multiples of 3. The receding half of the galaxy resides to the northwest. The velocity contours in velocity fields range from 680 km s^{-1} to 940 km s^{-1} in intervals of 20 km s^{-1}. Panels in the left column are at full resolution and panels in the right column are smoothed to 30″. The upper *x*-axis units apply only to the top two rows, while the lower *x*-axis units apply to the bottom row.

misses some extraplanar gas that happens to be at the same velocity (in projection) as the disk gas (F. Fraternali 2017, in preparation). This is particularly true for gas near the minor axis, where the rotation signal is weak. We conclude that overall the mass estimates for the extraplanar gas derived from the two methods are in reasonable agreement, and we find ∼10%–20% of the total H I mass to be extraplanar.

5.1. Relation of Extraplanar Gas to Star Formation

We incorporate two ancillary images—one Hα narrowband image, and one *GALEX* FUV image from Gil de Paz et al. (2007)—as tracers of star formation in NGC 4559. We show the extracted extraplanar gas overlaid as colored contours atop the Hα image and the *GALEX* FUV image in Figure 7. In Figure 7, we see the location of the highest densities of extraplanar H I. The three highest density contours (violet, blue, and green) trace the regions of active star formation. Additionally, a spiral arm feature seen extending to the southeast in both the Hα and FUV images is traced by the extraplanar gas. Note that there are some small isolated depressions in the extracted extraplanar gas. These are not in all cases regions with lesser amounts of extraplanar gas, but could be regions where the Gaussian profile fit did not converge.

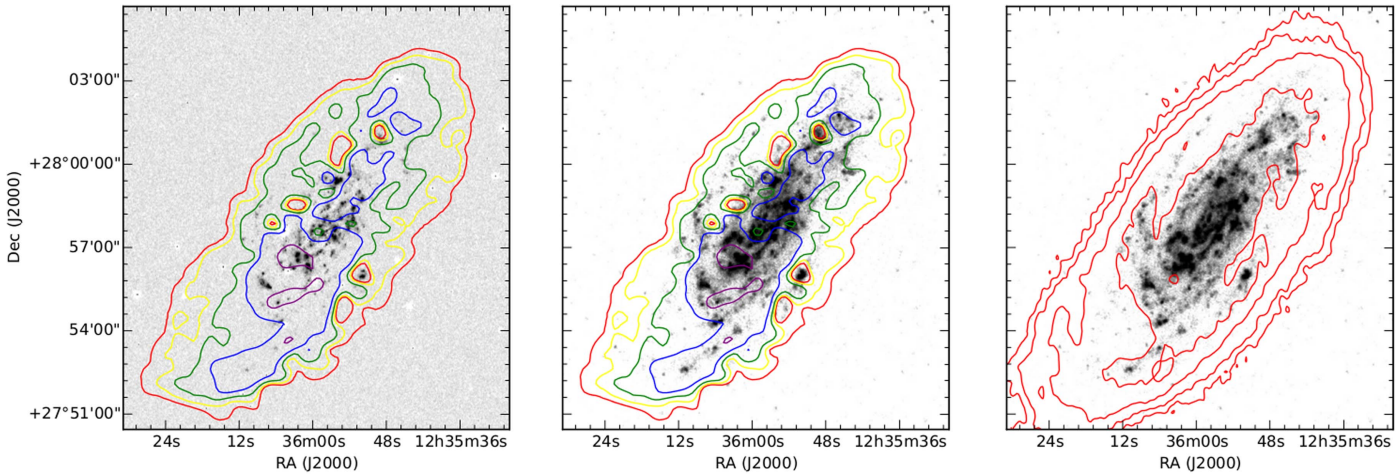

Figure 7. Left: KPNO Hα image, middle: *GALEX* FUV image (Gil de Paz et al. 2007), right: *GALEX* FUV image. Overlaid atop the left two images are the moment 0 contours of total extracted extraplanar gas. The colors represent different values of column density; from lowest to highest, these are red, yellow, green, blue, and violet. The contours begin at 3.75×10^{20} atoms cm^{-2} and increase in multiples of 2. Overlaid atop the rightmost image is the full-resolution H I data, the same as in Figure 1.

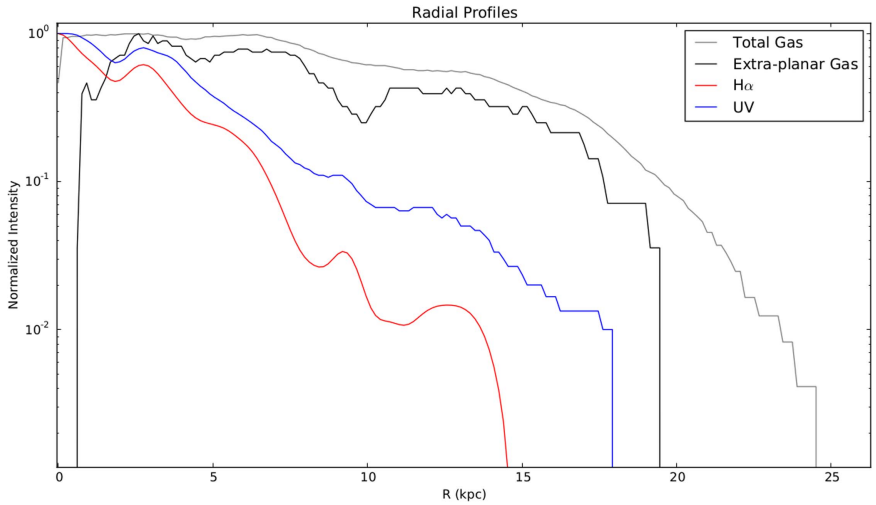

Figure 8. Radial profiles obtained from the extracted extraplanar gas, total H I map, Hα map, and *GALEX* UV map. The Hα and UV maps are smoothed to match the resolution of the H I map before the radial profiles are calculated. The intensities are normalized to their peak values so differences in profiles can be easily compared.

To better see the radial extent of the extraplanar gas and the tracers of star formation, we computed azimuthally averaged radial profiles for the total H I, Gaussian-extracted extraplanar gas cube, the Hα image, and the *GALEX* FUV image. All profiles are corrected for the inclination of the galaxy. These radial profiles are shown in Figure 8. In this figure, the intensity of each component has been normalized to its peak so that differences in structure can be seen more easily. We find that the total H I is more extended than the extraplanar gas. The extraplanar gas traces the extent of the UV profile well. Since UV emission, which is indicative of older star formation, and the extraplanar gas are coincident, it is likely that the extraplanar gas is related to past star formation processes (Kennicutt & Evans 2012). Had the extraplanar gas been due to accretion, there would be a high likelihood of seeing more radially extended extraplanar gas that traces the extent of the total H I. Thus, we conclude that the extraplanar gas is most likely due to star formation processes.

We also note that our modeling showed evidence that the value of thick-disk lag approached zero outside $R \sim 12$ kpc in the receding half. The modeled thick disk still contained gas there, so this gas would be nonlagging extraplanar gas that would not be found by the Gaussian fitting algorithm. However, we cannot distinguish this gas from disk gas observationally, due to the inclination of the galaxy, so we cannot say whether or not the thick-disk lag approaches zero outside this radius.

It is interesting that the lagging gas is still closely associated with the spiral arms (see, e.g., the southern spiral arm in Figure 7). Here, it is relevant to consider the timescale of the fountain cycle, which is the amount of time it takes for an ejected parcel of gas to fall back down onto the disk. If the ejection occurs at $\sim$70 km s^{-1} and is vertically stationary at its apex, then its average vertical velocity is $\sim$35 km s^{-1}. This vertical ejection velocity is consistent with the results of Fraternali & Binney (2006), where a vertical kick velocity of this magnitude was used in dynamical models matching observed extraplanar properties of NGC 891 and NGC 2403. If the gas reaches a vertical height of $\sim$2 kpc, then it will traverse the full vertical extent of 4 kpc and fall back to the disk in $\sim$100 Myr. When the gas is at a vertical height of 2 kpc it experiences a lag of 26 km s^{-1}, and while it is at 1 kpc it lags

the disk by 13 km s^{-1}. Thus, the average magnitude of the lag is 13 km s^{-1}, which would produce an azimuthal offset of ∼1.3 kpc over the course of the 100 Myr timescale of the fountain cycle. This is slightly larger than the 30″ (1.1 kpc) smoothed beam, which is most sensitive to features of diffuse lagging gas. Although the inclination of the galaxy would make this offset slightly smaller, we see no evidence for a systematic offset of 0.5–1 beam. The timescales suggest that the extraplanar gas is likely to be recently ejected fountain gas that has not had time to cool and begin its journey back down to the disk. So, we conclude that the most likely origin for the bulk of extraplanar H I in NGC 4559 is the galactic fountain mechanism; i.e., H I is transported above the disk as cold/warm gas in superbubbles following the explosion of supernovae.

Our results show roughly 10%–20% of the total H I mass to be extraplanar. A similar amount of extraplanar gas (∼10%) was found for NGC 2403 by Fraternali et al. (2002) using a similar Gaussian profile fitting and extraction to what is used in this study. Interestingly, NGC 2403 and NGC 4559 also have similar star formation rates (SFRs) of 1.0 $M_\odot$ yr^{-1} and 1.1 $M_\odot$ yr^{-1}, respectively (Sanders et al. 2003). Additionally, NGC 3198 was found to house ∼15% of its total H I mass as extraplanar gas, with an SFR of 0.61 $M_\odot$ yr^{-1} (Gentile et al. 2013). The amount of extraplanar gas in NGC 3198 comes from an analysis with a tilted ring model, in which 15% of the total H I mass is used in a thick-disk component. Since some of that thick disk is superimposed on the thin disk, the amount of extraplanar gas in NGC 3198 is likely closer to ∼10%, as we find in NGC 4559. Indeed, even when star formation rate density (SFR/D_{25}^2) is compared, NGC 2403 and NGC 4559 are similar, with star formation rate densities of 0.045 and 0.042 $M_\odot$ yr^{-1} kpc^{-2} (Sanders et al. 2003). NGC 3198 has a lower star formation rate density of 0.016 $M_\odot$ yr^{-1} kpc^{-2} (Sanders et al. 2003), yet still has a substantial amount of extraplanar gas (Gentile et al. 2013).

5.2. Forbidden Gas and H I Holes

A striking amount of anomalous gas located in the "forbidden" region of the position–velocity diagram along the major axis is present in the data cube of NGC 4559. This feature was also mentioned in B05, but the deeper HALOGAS data make it possible to study this region in more detail. The existence of other H I holes is noted in this galaxy. However, we focus on this particular one because of its proximity to the forbidden gas feature.

A study by Boomsma et al. (2008) found that most of the H I holes in NGC 6946 are related to extraplanar material expelled by star formation. The previous study by B05 noted the potential relationship between the gas feature at forbidden velocity in NGC 4559 and a nearby H I hole. The same H I hole is visible in the full-resolution HALOGAS cube as well. In Figure 9, we show the sum of nine channels in the full-resolution HALOGAS cube that showed the strongest forbidden emission, overlaid on the *GALEX* FUV image, and mark the locations of the H I hole and forbidden velocity filament. We estimate the location of the center of this hole to be $\alpha = 12^h36^m3\overset{s}{.}3$, $\delta = 27°57'9\overset{''}{.}6$, which is in good agreement with B05. We estimate the center of the forbidden gas feature to be located at $\alpha = 12^h36^m0\overset{s}{.}6$, $\delta = 27°56'52\overset{''}{.}0$—this is ∼40″ (1.5 kpc) away from the center of the hole on the sky. Assuming that the hole and the forbidden gas feature lie in the same plane on the sky, the vertical distance from the forbidden gas to the point on the plane directly below it would be $h = 1.5$ kpc tan(67°) = 3.5 kpc.

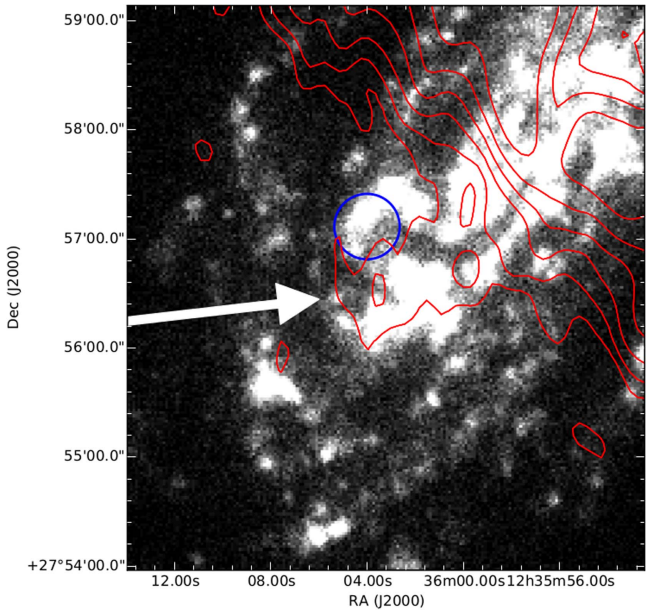

Figure 9. Background image: *GALEX* FUV image; red contours: integrated nine channels in the full-resolution cube containing forbidden gas emission. The blue circle outlines the position of the large H I hole. The arrow points to the forbidden gas filament. The contour levels begin at 3 times the rms noise in a single channel and increase in multiples of 3.

In order to explore the potential origins of this peculiar feature, we extracted it from each channel in which it is present in the 30″ smoothed cube. Emission was found in 13 channels between 817.78 km s^{-1} and 867.20 km s^{-1}. The total mass of the feature is ∼1.4 × 10^6 $M_\odot$.

The proximity and orientation of the forbidden gas filament suggests that it could contain gas that may once have filled the hole. Assuming that the bulk motion of the gas in the forbidden filament can be characterized by the velocity of the central channel of its emission, we estimate the velocity of the filament relative to the gas in its spatial surroundings. The central channel of the filament's emission is at 842.5 km s^{-1}, and the channel containing most of the gas spatially coincident with the feature is at 719 km s^{-1}, i.e., the bulk velocity of the gas around the filament has a velocity of ∼123 km s^{-1} relative to the hole. We estimate the amount of kinetic energy the forbidden feature would have moving directly vertically from the plane of the galaxy via $K = (1/2)mv^2$. Using the relative velocity of the feature corrected for inclination, this energy would be ∼1.8 × 10^{53} erg.

We estimate the potential energy required to move a parcel of gas to the height of the feature, assuming it is located directly above the plane of the disk (3.5 kpc). We use Equation (4) of Howk & Savage (1997) for the potential energy of extraplanar clouds above a galactic disk. We use the above tabulated cloud mass and height above the plane, assume that the scale height of the stellar disk is the scale height of the model thin disk of ∼200 pc, and assume the midplane mass density is that of the solar neighborhood: $\rho_0 = 0.185\,M_\odot$ pc^{-3} (Bahcall 1984). We find that the corresponding potential energy of the forbidden gas feature is 2 × 10^{53} erg s^{-1}. The total energy—kinetic plus potential—required to move this gas is ∼4.0 × 10^{53} erg, or the energy of ∼2000 supernovae of energy 10^{51} erg each, assuming 20% efficiency. This efficiency

and energy requirement are reasonable for a superbubble that arose from many supernovae. Fraternali et al. (2015) relate the Galactic HVC Complex C to ejection via star formation processes within the Milky Way. This complex has a hydrogen mass and relative velocity both roughly twice as large as seen in the forbidden gas feature of NGC 4559. Fraternali et al. (2015) estimate the number of supernovae required to eject the complex to be $\sim 1 \times 10^4$, corresponding to a typical star formation rate density of a star-forming region in the disk of the Milky Way. Thus, it is plausible that this feature in NGC 4559 was once part of the disk, but was ejected through star formation processes.

If our assumptions about the vertical separation of the forbidden gas from the disk were incorrect, the energy calculation would change somewhat. The kinetic energy would be unchanged. However, the potential energy would decrease if the gas were actually closer to the disk, further bolstering our above conclusion. If the gas were actually located further from the disk, it would require more supernovae to potentially eject the forbidden gas feature. If the gas were located 7 kpc above the disk, this would increase our potential energy calculation by a factor of 5, which would not be enough to change the above conclusion. Of course, beyond some height, the potential energy required would begin to become unreasonably high. But the greater the height of the gas, the less likely it is to show the smooth kinematic connection to gas of permitted velocity in the *p–v* diagram along the major axis.

We can explore whether or not the forbidden gas is an outflow feature or infalling by using purely geometric arguments. Both the hole and the forbidden gas feature are located near the major axis in the approaching side of the galaxy and we assume that the spiral arms seen in the *GALEX* image are trailing arms (see Figure 9), indicative of counter-clockwise rotation. If the arms are indeed trailing arms, then the southwest side is the near side. If we assume that the spatial separation between the hole and the forbidden gas feature is mostly along the *z*-axis, then the feature must be located *on the far side* of the disk, and is therefore outflowing due to its positive heliocentric velocity. If it is inflowing and on the near side of the disk, then the feature cannot be located above the hole, but would instead be "ahead" of the hole in azimuth, which cannot be due to a lag. Therefore, if the feature is inflowing, it is either not related to the hole or was launched from the hole at a large angle, which is not likely. Since we see this forbidden gas feature as a smooth connection to the signatures of extraplanar gas at permitted velocities, which we attribute to a galactic fountain, we believe the forbidden gas feature to most likely be an outflow on the far side of the disk.

In an attempt to explain the presence of the forbidden gas feature, numerous tilted ring models containing both radial and vertical inflows and outflows were created with TiRiFiC. Models were created containing varying strengths of these flows in the inner regions of the thick and thin disks of the best-fitting thick-disk model. However, no combination of these effects made models containing any distinct feature akin to the forbidden gas feature. Simple kinematic changes to the tilted ring model are insufficient to match the observed phenomenon. This may be due to the nature of tilted ring fitting—we attempted to model an isolated, non-axisymmetric structure within rings that extend through half of the angular extent of the entire galaxy. We note that Fraternali & Binney (2006) show that a random fountain can produce similar, centrally located, forbidden gas features that also exist in NGC 2403.

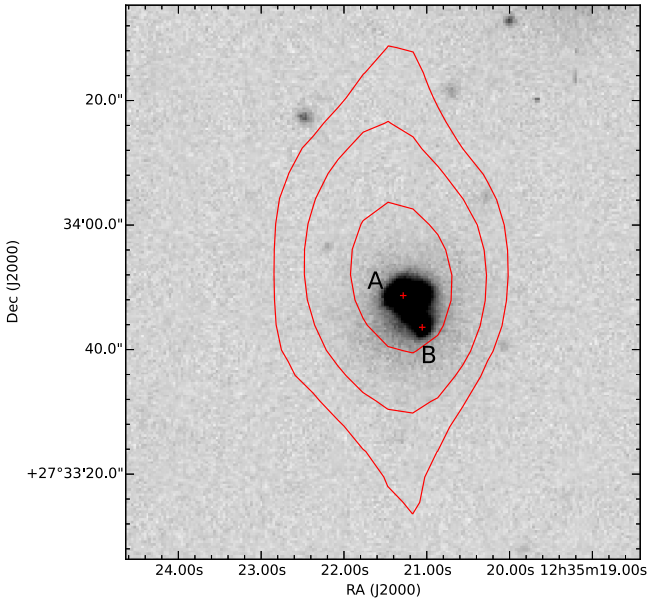

Figure 10. SDSS *g*-band overlaid with red H I contours. The contour levels begin at 2.4×10^{19} cm^{-2} and increase in multiples of 2. The red crosses mark the positions of the two SDSS sources: point A is the northeastern source, and point B is the southwestern source. The object is a point source in H I, so the object's shape traces the beam.

6. H I Dwarf Galaxy

A dwarf galaxy previously undetected in H I was found in the HALOGAS data cube of NGC 4559 with the widest field. The center of this dwarf is located at $\alpha = 12^{\rm h}35^{\rm m}21\overset{\rm s}{.}335$, $\delta = 27°33'46\overset{''}{.}68$, which puts it at least $0\overset{\circ}{.}418$ (∼58 kpc) away from the center of NGC 4559, if the objects are spatially aligned in the same plane. The heliocentric velocity of the dwarf is ∼1200 km s^{-1} and emission from the dwarf spans nine channels from 1187–1224 km s^{-1} in total. This also places the dwarf well outside the field of view of the Hα image. Velocities are computed in the optical definition. The total H I flux of this feature was found to be 27.1 mJy, corresponding to a total H I mass of $\sim 4 \times 10^5\, M_\odot$, assuming a distance to the dwarf of 7.9 Mpc. We show the H I dwarf in Figure 10, overlaid on a *g*-band image from the Sloan Digital Sky Survey (SDSS).

We attempted to determine whether the dwarf is, in fact, a bound companion to NGC 4559. The circular velocity of NGC 4559 is ∼130 km s^{-1}, as seen in the H I rotation curve modeled in this study. We assume a typical halo mass for a galaxy at the rotation velocity of NGC 4559 by inverting Equation (8) in Klypin et al. (2011). That study found an empirical relation between circular velocity and halo mass, assuming Navarro–Frenk–White dark-matter density profiles using the Bolshoi simulation. The virial mass we find is $\sim 2.8 \times 10^{11}\, M_\odot$, assuming $h = 0.70$ also from the Bolshoi simulation (Klypin et al. 2011). We find the virial mass of a Milky Way-sized halo to be $\sim 1.5 \times 10^{12}\, M_\odot$ using that same relation. Since $R_{\rm vir} \propto M_{\rm vir}^{1/3}$, we estimate the virial radius of NGC 4559 to be ∼170 kpc. Even if the dwarf is not in the same plane as NGC 4559, it is still likely well within the virial radius.

We estimate the escape velocity of the dwarf using Equation (2-192) in Binney & Tremaine (1987). We estimate

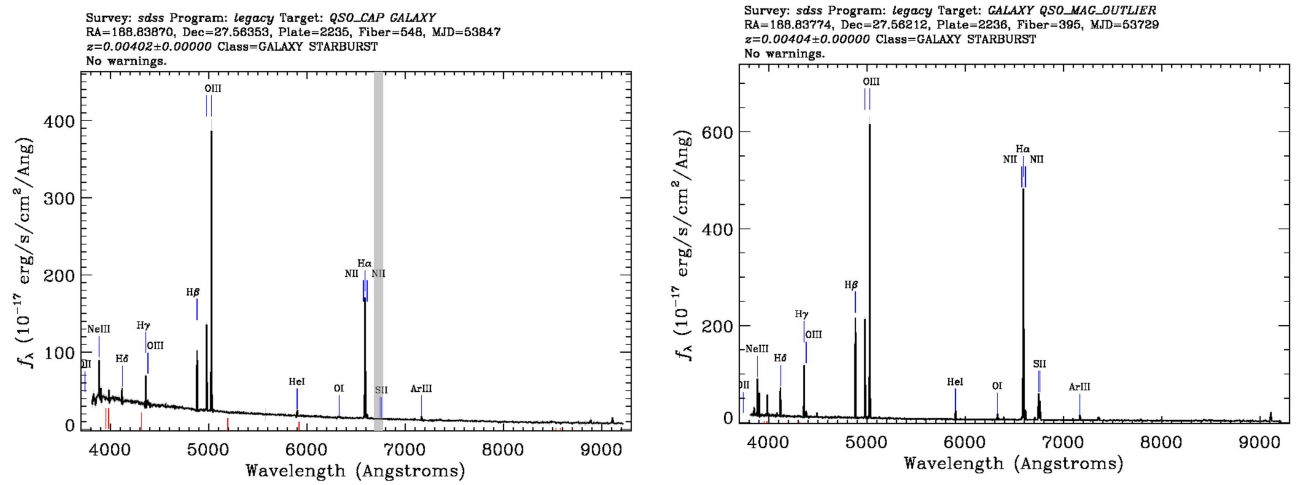

Figure 11. SDSS spectra of the two regions associated with the BCD galaxy. The left panel shows the northeastern region (A), and the right panel the southwestern region (B). The vertical gray band encompasses masked pixels in the spectrograph. The blue and red lines point out the locations of possible emission and stellar absorption lines, respectively.

$r_\star \sim 25$ kpc, the maximum radius where the circular velocity is constant. Since the halo extends further than the H I emission, this value is a lower limit, and thus makes the estimate of escape velocity also a lower limit. In this calculation, we also use the estimate of circular velocity from the tilted ring modeling ($v_c \sim 130\,\mathrm{km\,s^{-1}}$) and the assumed distance to the dwarf of 58 kpc. This yields an escape velocity of $v_{\rm esc} \sim 121\,\mathrm{km\,s^{-1}}$. This value is much lower than the difference of $390\,\mathrm{km\,s^{-1}}$ between the systemic velocity of NGC 4559 and the central velocity of the dwarf. Though we cannot measure the exact distance where the rotation curve ceases to be flat, it would have to occur at a radial distance of ∼261 kpc for the escape velocity to match the velocity of the dwarf. Since it is unlikely that the rotation curve is flat to such an extreme distance, we conclude that the dwarf is unbound.

Two optical counterparts for this object were found in the SDSS (Eisenstein et al. 2011) data release 12 database. In Figure 10 we show an SDSS g-band image with the HALOGAS H I contours overlaid in red, showing the locations of the SDSS counterparts and the source in H I. These two objects are separated by ∼5″ and appear to be merging. The SDSS spectra for these two regions show the objects to both reside at $z = 0.004$, which corresponds to a heliocentric velocity of $1198\,\mathrm{km\,s^{-1}}$, which is effectively identical to the velocity of the dwarf in H I. The spectra of these objects can be seen in Figure 11. They both show large O III/Hβ ratios, implying the existence of high-excitation H II regions, and the existence of young stars. We conclude that the dwarf is actually two merging blue compact dwarf (BCD) galaxies.

The SDSS-quoted u- and g-band magnitudes for the northeastern object are 17.12 and 16.67, and those for the southwestern object are 17.22 and 16.79. Using the assumed distance of 7.9 Mpc, the corresponding absolute magnitudes are $M_u = -12.4$ and $M_g = -12.8$ for the northeastern object, and $M_u = -12.3$ and $M_g = -12.7$ for the southwestern object. We converted these magnitudes to an equivalent B-band magnitude, then calculated the luminosity of the objects assuming that they are at the same distance as NGC 4559. The dwarves have an H I mass-to-blue-light ratio of 0.18. The optical size of the companion is ∼5″ or 191.5 pc, assuming that the object is at the distance of the galaxy. This H I mass-to-blue-light ratio is low, but within the values obtained by Huchtmeier et al. (2007)—an Effelsberg H I study of 69 BCD galaxies. The combined H I mass of these dwarves is also of the same order of magnitude as that of 12 dwarf galaxies in the Local Group as described in McConnachie (2012). Of these 12, only four are within 200 kpc of their parent galaxy. Also of these 12, five have M_V between −14 and −11.

7. Discussion and Conclusions

Our analysis of the extraplanar H I in NGC 4559 can be compared to work on other moderately inclined spiral galaxies in the HALOGAS sample. In a similar study by Gentile et al. (2013) of NGC 3198, a lagging extraplanar H I component was discovered, containing ∼15% of the total H I mass of that galaxy. The extraplanar H I in NGC 3198 was found to be characterized by a thick-disk scale height of ∼3 kpc with a vertical lag of 7–15 $\mathrm{km\,s^{-1}\,kpc^{-1}}$. These values are very similar to what was found in NGC 4559.

NGC 2403 is a very similar galaxy to NGC 4559 in morphology and star formation characteristics, and was studied in H I with the Very Large Array by Fraternali et al. (2002). NGC 2403 has a star formation rate of $1\,M_\odot\,\mathrm{yr^{-1}}$ (Sanders et al. 2003) and a rotation velocity of $122\,\mathrm{km\,s^{-1}}$. Fraternali et al. (2002) found NGC 2403 to contain an extraplanar H I component containing ∼10% of the total H I mass of that galaxy. That study found the extraplanar H I to be lagging the disk's rotation velocity by 25–50 $\mathrm{km\,s^{-1}}$.

A recent study by de Blok et al. (2014) of NGC 4414 found that only about ∼4% of the total H I mass is in extraplanar gas. However, due to the disturbed nature of that galaxy's halo, that number is difficult to constrain. Analysis of the inner disk of NGC 4414 shows that galaxy has likely experienced a recent interaction with a dwarf galaxy, which may account for its large star formation rate of 4.2 $M_\odot\,\mathrm{yr^{-1}}$.

Although the characteristics of the extraplanar H I in NGC 4559 seem to fit into the overall picture of a nearby, moderately inclined spiral galaxy, it is difficult to say whether or not lagging extraplanar H I is ubiquitous or extraordinary throughout the nearby universe. Furthermore, is extraplanar lagging H I always seen to be likely caused by the galactic fountain mechanism? Greater understanding of this problem can be obtained through further study of the entire HALOGAS

sample, both edge-on and moderately inclined galaxies. The next generation of radio telescopes, including the Square Kilometre Array, will answer these questions in the future.

We used the deep 21 cm HALOGAS observations of NGC 4559 to expand upon the work done by Barbieri et al. (2005) in characterizing diffuse extraplanar and anomalous characteristics in the H I distribution of that galaxy. We created detailed three-dimensional, tilted ring models of that galaxy's H I. We confirm B05, in that a model containing only a ∼200 pc thin disk cannot produce a fit to the faint signatures of extraplanar lagging gas seen in this galaxy. We create an expanded model containing a thick disk comprising 20% of the total H I of the thin-disk model, whose thick-disk component extends vertically to a scale height of 2 kpc. We constrain the magnitude of the gradient in rotation velocity with height in a simple thick-disk model to be $\sim 13\,\mathrm{km\,s^{-1}\,kpc^{-1}}$ in the approaching side and $\sim 6.5\,\mathrm{km\,s^{-1}\,kpc^{-1}}$ in the receding side. In the fine-tuned model, we find a lag of $\sim 13\,\mathrm{km\,s^{-1}\,kpc^{-1}}$ in both halves, but with a cutoff in the receding half near R_{25} is an improved match to the data. This measurement of the lag magnitude was not previously done in B05, where a separate rotation curve was used for the thick disk.

We use a Gaussian line profile fitting technique to extract the anomalously rotating extraplanar gas from the normally rotating disk. In this technique we find that ∼10% of the total H I mass is extraplanar. Also, the extraplanar gas is localized to the inner star-forming regions of the galaxy, again suggesting that the bulk of this gas is of galactic fountain origin.

We analyze the spatial locations of total and extraplanar H I in relation to Hα emission seen from young stars as a tracer for active star formation. We find that extraplanar H I traces regions of star formation, leading us to conclude that most of the extraplanar H I seen is from in situ star formation, i.e., a galaxy-wide galactic fountain.

To further build on the work of B05, we extracted the emission from a filament of H I located in the kinematically forbidden region of the position–velocity diagram along the major axis. We find that the feature contains $1.4 \times 10^6\,M_\odot$ of H I. Energy estimates of the feature require ∼2000 supernovae to move the gas, which is consistent with a superbubble or other in situ processes due to star formation. The remarkable proximity of this feature to a large H I hole is difficult to ignore, but no irrefutable evidence tying the two together was found. Furthermore, the feature extends into the signatures of extraplanar gas quite smoothly in the position–velocity diagram along the major axis, further pointing to the filament originating inside the normally rotating disk and being expelled through star formation.

We analyze a merger of two BCD galaxies, previously unobserved in H I, located ∼0.°4 from the center of NGC 4559. The BCD galaxies contain $\sim 4 \times 10^5\,M_\odot$ of H I and also contain two spatially tight counterpart sources in SDSS. We conclude that the objects are merging BCD galaxies, due to a low H I mass-to-blue-light ratio of 0.18 and spectra largely indicative of H II regions.

This material is based upon work supported by the National Science Foundation Graduate Research Fellowship under Grant No. 127229 to C.J.V. This material is also based on work partially supported by the National Science Foundation under Grant No. AST-1616513 to R.J.R. and Grant Nos. AST-0908126 and AST-1615594 to R.A.M.W. This project has received funding from the European Research Council (ERC) under the European Union's Horizon 2020 research and innovation programme (grant agreement No 679627). We would like to thank the anonymous referee for insightful and helpful comments that led to the overall improvement of this work.

References

Bahcall, J. N. 1984, ApJ, 276, 169
Barbieri, C. V., Fraternali, F., Oosterloo, T., et al. 2005, A&A, 439, 947
Benjamin, R. A. 2002, in ASP Conf. Ser. 276, Seeing Through the Dust: The Detection of HI and the Exploration of the ISM in Galaxies, ed. A. R. Taylor, T. L. Landecker, & A. G. Willis (San Francisco, CA: ASP), 201
Binney, J., & Tremaine, S. 1987, Galactic Dynamics (Princeton, NJ: Princeton Univ. Press)
Boomsma, R., Oosterloo, T. A., Fraternali, F., van der Hulst, J. M., & Sancisi, R. 2008, A&A, 490, 555
Bregman, J. N. 1980, ApJ, 236, 577
Broeils, A. H. 1992, PhD thesis, Univ. Groningen 1992
Collins, J. A., Benjamin, R. A., & Rand, R. J. 2002, ApJ, 578, 98
Corbelli, E., & Salpeter, E. E. 1993, ApJ, 419, 104
de Blok, W. J. G., Józsa, G. I. G., Patterson, M., et al. 2014, A&A, 566, 80
Eisenstein, D. J., Weinberg, D. H., Agol, E., et al. 2011, AJ, 142, 72
Fraternali, F., & Binney, J. J. 2006, MNRAS, 366, 449
Fraternali, F., Marasco, A., Armillotta, L., & Marinacci, F. 2015, MNRAS, 447, L70
Fraternali, F., van Moorsel, G., Sancisi, R., & Oosterloo, T. 2002, AJ, 123, 3124
Gentile, G., Józsa, G. I. G., Serra, P., et al. 2013, A&A, 554, A125
Gil de Paz, A., Boissier, S., Madore, B. F., et al. 2007, ApJS, 173, 185
Heald, G., de Blok, W. J. G., Lucero, D., et al. 2016, MNRAS, 462, 1238
Heald, G., Józsa, G., Serra, P., et al. 2011, A&A, 526, A118
Howk, J. C., & Savage, B. D. 1997, AJ, 114, 2463
Howk, J. C., & Savage, B. D. 1999, AJ, 117, 2077
Huchtmeier, W. K., Petrosian, A., Gopal-Krishna, & Kunth, D. 2007, A&A, 462, 919
Irwin, J., Beck, R., Benjamin, R. A., et al. 2012, AJ, 144, 43
Józsa, G. I. G., Kenn, F., Klein, U., & Oosterloo, T. A. 2007, A&A, 468, 731
Kamphuis, P., Peletier, R. F., Dettmar, R.-J., et al. 2007, A&A, 468, 951
Kennicutt, R. C., & Evans, N. J. 2012, ARA&A, 50, 531
Klypin, A. A., Trujillo-Gomez, S., & Primack, J. 2011, ApJ, 740, 102
Maloney, P. 1993, ApJ, 414, 41
Marinacci, F., Fraternali, F., Nipoti, C., et al. 2011, MNRAS, 415, 1534
McConnachie, A. W. 2012, AJ, 144, 4
Oosterloo, T., Fraternali, F., & Sancisi, R. 2007, AJ, 134, 1019
Putman, M. E., Peek, J. E. G., & Joung, M. R. 2012, ARA&A, 50, 491
Rossa, J., & Dettmar, R.-J. 2003, A&A, 406, 493
Sanders, D. B., Mazzarella, J. M., Kim, D.-C., Surace, J. A., & Soifer, B. T. 2003, AJ, 126, 1607
Sault, R. J., Teuben, P. J., & Wright, M. C. H. 1995, in ASP Conf. Ser. 77, Astronomical Data Analysis Software and Systems IV, ed. R. A. Shaw, H. E. Payne, & J. J. E. Hayes (San Francisco, CA: ASP), 433
Shapiro, P. R., & Field, G. B. 1976, ApJ, 205, 762
Shostak, G. S. 1975, ApJ, 198, 527
Tüllmann, R., Pietsch, W., Rossa, J., Breitschwerdt, D., & Dettmar, R.-J. 2006, A&A, 448, 43
van der Hulst, J. M., Terlouw, J. P., Begeman, K. G., Zwitser, W., & Roelfsema, P. R. 1992, in ASP Conf. Ser. 25, Astronomical Data Analysis Software and Systems I, ed. D. M. Worrall, C. Biemesderfer, & J. Barnes (San Francisco, CA: ASP), 131
Zschaechner, L. K., Rand, R. J., & Walterbos, R. 2015, ApJ, 799, 61